Multiparticle production in a two-component dual parton model

P. Aurenche
Laboratoire de Physique des Particules, Institut Nacional de Physique Nucléare et de Physique des Particules, Annecy, France

F. W. Bopp
Fachbereich Physik, Universität Siegen, Siegen, Federal Republic of Germany

A. Capella
Laboratoire de Physique Théorique et Hautes Energies, Université de Paris XI, Orsay, France

J. Kwiecinski
Institute of Nuclear Physics, Krakow, Poland

M. Maire
Laboratoire de Physique des Particules, Institut Nacional de Physique Nucléare et de Physique des Particules, Annecy, France

J. Ranft* and J. Tran Thanh Van
Laboratoire de Physique Théorique et Hautes Energies, Université de Paris XI, Orsay, France
(Received 7 May 1991)

The dual parton model (DPM) describes soft and semihard multiparticle production. The version of the DPM presented in this paper includes soft and hard mechanisms as well as diffractive processes. The model is formulated as a Monte Carlo event generator. We calculate in this model, in the energy range of the hadron colliders, rapidity distributions and the rise of the rapidity plateau with the collision energy, transverse-momentum distributions and the rise of average transverse momenta with the collision energy, multiplicity distributions in different pseudorapidity regions, and transverse-energy distributions. For most of these quantities we find a reasonable agreement with experimental data.

PACS number(s): 13.85.Hd, 12.40.Aa, 12.40.Lk

I. INTRODUCTION

The present situation in high energy physics is characterized by the trend to study the interaction of elementary particles at ever increasing energies. Several hadron colliders in the TeV energy range are under construction or under intense discussion.

The theoretical models to study hadronic multiparticle production processes at the energies of existing and future accelerators have changed several times during the last decades. During the 1970's models which implemented the concept of Feynman-scaling [1] were favored. The experiments at the CERN ISR and SPS colliders in the 1980's showed however that Feynman scaling is not realized by nature. Therefore models for inelastic hadronic reactions which do not show Feynman scaling were studied. The most important feature is a rapidity plateau slowly rising with the collision energy. Furthermore, models which start in their construction from quark-parton ideas are now preferred.

Hadronic multiparticle production is nonperturbative in nature and unfortunately cannot be studied with perturbative QCD. Models for multiparticle production therefore use concepts such as the Pomeron, and these models are expected to be explained eventually by QCD. At present, there exist several attempts to derive the Pomeron from QCD [2], but this connection is not yet completely clear.

Soft multiparticle production in hadron-hadron collisions in the framework of the dual parton model (DPM) has been studied since the beginning of the 1980's by several groups [3–7]. The DPM is very successful in explaining the non-Feynman-scaling behavior of the data and also the deviations from Koba-Nielsen-Olsen (KNO) scaling behavior [8] of multiplicity distributions.

Experiments at the proton-antiproton colliders furthermore indicated that hard and soft production processes are closely related. The best known of these experiments are the observation of correlations between the average transverse momenta of hadrons produced and the charged multiplicity of produced hadrons [9], the observation of "minijets" in hadronic collisions, and changes of the properties of the underlying soft events in data samples with jets or minijets [10].

These experiments can be explained by perturbative hard or semihard constituent scattering. The same constituent scattering is also responsible for at least part of the rise of the hadronic cross sections with energy. This was studied quantitatively in papers by Capella, Tran Thanh Van, and Kwiecinski [11] and Durand and Pi [12]. In these papers the consequences for the total and inelastic cross sections of the unitarization of soft and hard

*Permanent address: Sektion Physik, Universität Leipzig, Leipzig, FRG.

scattering cross sections were studied.

A preliminary Monte Carlo description of the two-component DPM incorporating soft hadronic processes, described by the supercritical Pomeron, and semihard processes, described by perturbative constituent scattering, was given by Ranft *et al.* [13]. In [14] the perturbative hard scattering component of the model was studied in more detail. Different kinds of correlations were studied within this model recently in a paper by Bopp *et al.* [15] as well as in a previous version of the model [16]. The model is implemented in the form of the Monte Carlo code DTUJET [17–19].

The models in [13] and [14] contain only the soft and semihard components. In the present paper we include in addition also high-mass diffractive processes, which are described by diagrams containing the triple-Pomeron coupling, and low-mass diffractive processes, described using a two-channel eikonal method.

In Sec. II and in the Appendixes we give a description of the model. In Sec. III various average properties and distributions are calculated within the model in the energy range of hadron colliders and compared to experimental data. In Sec. IV we give a summary.

II. THE TWO-COMPONENT DUAL PARTON MODEL INCLUDING DIFFRACTIVE PROCESSES

A. Construction of the model

In this section we will discuss the basic ideas of the dual parton model and the way in which the hard component and a diffractive component is included. Many technical details related to this section are given in Appendixes A and B.

The two most important components of the model are the soft component, described by the supercritical Pomeron and the hard component, described by perturbative QCD (the hard Pomeron).

At higher energies the hadron-hadron interaction is dominated by Pomeron exchange. The Pomeron is cut into two chains (or strings) and these chains are connected to the hadron constituents. In the leading order the proton consists of one valence quark and one valence diquark and the interaction between the hadrons gives rise to two chains which are stretched between these constituents. Figure 1(a) shows the leading diagram (one cut Pomeron) for a pure soft p-$\bar{p}$ collision.

The Pomeron exchange corresponds to a pure soft cross section and can be parametrized as the so-called supercritical Pomeron. The cross section corresponding to the supercritical Pomeron is given in Appendix A1. We use the parameters as obtained by Capella, Tran Thanh Van, and Kwiecinski [11].

The hard scattering input cross section as calculated in the QCD parton model for a lower transverse-momentum cut $p_{\perp,\min}=2$ or 3 GeV/c is given in Appendix A3.

Both the hard σ_h and the soft σ_s input cross sections increase with energy practically like powers of s whereas the total cross section is proportional to $(\ln s)^2$ so that the input cross sections exceed the total cross section $\sigma_{\rm tot}$ at higher energies. The average multiplicities of hard and soft scatterings in an inelastic event are $\langle n_h \rangle = \sigma_h/\sigma_{\rm inel}$ and $\langle n_s \rangle = \sigma_s/\sigma_{\rm inel}$, respectively. These multiplicities increase with energy and at higher $\sqrt{s}$ a sizable part of events has more than one hard or soft scattering. The multiplicities are calculated with an unitarization scheme [11] which makes use of the Abramovski-Gribov-Kancheli (AGK) cutting rules [20]. This scheme gives the weights for events with i soft and j hard scatterings [13].

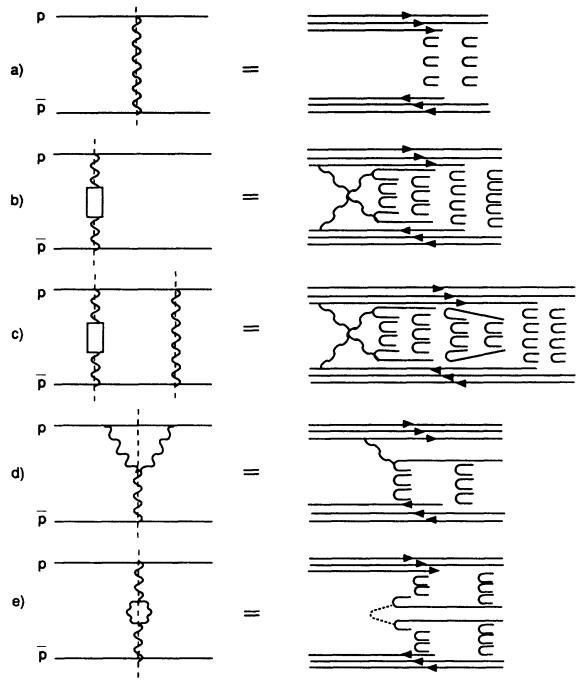

FIG. 1. Diagrams for the exchange of soft, hard, diffractive, and double-diffractive chains (a) one soft cut Pomeron (two soft chains); (b) one hard cut Pomeron (two soft and two hard chains), we always get soft chains in addition to the hard chains resulting directly from the parton-parton scattering; (c) one soft and one hard cut Pomeron (four soft, two hard chains); (d) one diffractively cut triple-Pomeron graph; (e) one cut Pomeron-loop graph (double diffraction).

In Fig. 1(b) we show a cut hard Pomeron. We always get soft chains in addition to the hard chains resulting from the parton-parton scattering. Here two gluons undergo a hard $2\rightarrow 2$ scattering and the resulting gluons which have transverse momenta $p_\perp \geq p_{\perp,\min}$ are split into quark-antiquark pairs. In Fig. 1(c) we give an example how a hard component is added to the leading pure soft diagram.

There are contributions with more than one hard scattering. These hard scatterings are mostly independent of each other and the only interconnection is the sharing of energy and momentum of the incoming hadrons. The hard (soft) component causes an increase of the average multiplicity of produced hadrons with energy due to the increase of the number of hard (soft) scatterings $n_h(n_s)$.

In addition to the hard and the soft components [Fig. 2(a) and Fig. 2(b)], we introduce furthermore the triple-Pomeron graph and a triple-Pomeron loop graph into the unitarization scheme; see Figs. 2(c) and 2(d). The simplest cut of the triple-Pomeron graph gives high-mass

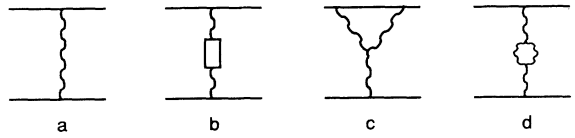

FIG. 2. The graphs representing the exchange of (a) soft Pomerons and (b) hard Pomerons, (c) the triple-Pomeron graph, and (d) a graph with a Pomeron loop.

single-diffractive events and the simplest cut of the loop graph gives high-mass double-diffractive events.

We introduce the input cross sections corresponding to the four different mechanisms in the impact-parameter representation:

$$\chi_i(B,s)=\frac{\sigma_1}{8\pi b_i}\exp\left[-\frac{B^2}{4b_i}\right] . \tag{2.1}$$

Here i stands for any one of the four inputs: s, the soft cross section; h, the hard cross section; TP, the triple-Pomeron cross section; and l, the loop cross section (see Appendix A2). The expressions of σ_i are given in Appendix A1. From Eq. (2.1) we get

$$\int 2\chi_i(B,s)d^2B=\sigma_i . \tag{2.2}$$

With this, in the impact-parameter representation we obtain the exclusive cross sections with l_c cut soft Pomerons, m_c cut hard Pomerons, m_c cut triple-Pomeron graphs, and p_c cut loop graphs:

$$\sigma(l_c,m_c,n_c,p_c,B,s)=\frac{(2\chi_s)^{l_c}}{l_c!}\frac{(2\chi_h)^{m_c}}{m_c!}\frac{(-2\chi_{\mathrm{TP}})^{n_c}}{n_c!}\times\frac{(-2\chi_L)^{p_c}}{p_c!}e^{-2\chi(B,s)} , \tag{2.3}$$

where $\chi(B,s)$ is given in Appendix B1. Numerical integration over the impact parameter B yields the exclusive multi-Pomeron cross sections $\sigma(l_c,m_c,n_c,p_c)$. These are the cross sections, which we need for the construction of inelastic events in the dual parton model.

The expressions for the total, inelastic, etc., cross sections are given in Appendix B1. The total cross section, for instance, is given by

$$\sigma_{\mathrm{tot}}=4\pi\int_0^\infty B\,dB(1-e^{-\chi(B,s)}) . \tag{2.4}$$

The hadronization of the l_c cut soft Pomerons and the m_c cut hard Pomerons has been described above; see Fig. 1. The hadronization of the n_c cut triple-Pomeron graphs and the p_c cut loop graphs is more complicated, since these graphs can be cut in different ways. Let us discuss this for the triple-Pomeron graph. One can distinguish the three different types of cuts of the triple-Pomeron graph, which are given in Fig. 3. We suppose, out of the n_c cut triple-Pomeron graphs α are cut like in Fig. 3(a), β are cut like in Fig. 3(b), and $n_c-\alpha-\beta$ are cut like in Fig. 3(c). We get according to the AGK cutting rules [20] the corresponding cross sections

$$\sigma^{\alpha,\beta}(l_c,m_c,n_c,p_c,B,s)=\sigma(l_c,m_c,n_c,p_c,B,s)\binom{n_c}{\alpha}\binom{n_c-\alpha}{\beta}(-2)^\alpha 4^\beta(-1)^{n_c-\alpha-\beta} . \tag{2.5}$$

Notice that the sum

$$\sum_{\alpha=0}^{n_c}\sum_{\beta=0}^{n_c-\alpha}\sigma_{\alpha\beta}(l_c,m_c,n_c,p_c,B,s)=\sigma(l_c,m_c,n_c,p_c,B,s) . \tag{2.6}$$

The treatment of the loop graph is completely equivalent to that of the triple-Pomeron graph.

In fact, since the triple-Pomeron coupling is small, it is sufficient to treat the single-diffractive and loop contributions to first order. But this is also necessary. Using the triple-Pomeron and loop graphs up to higher order in the eikonal framework used above would be inconsistent, since we would include only higher-order graphs of one special class such as those given in Fig. 4(a) and not graphs such as the ones given in Fig. 4(b) which in a consistent treatment should also be included up to the same number of loops. A consistent treatment of all enhanced graphs has been given in Ref. [21]. However, the resulting formalism is too cumbersome to be applied to the multiparticle production.

The last component of the model to be described is low-mass diffraction, which is introduced via a two-channel eikonal formalism. The corresponding equations are given in Appendix B2, the formalism is similar to the one already described, however somewhat more involved.

The introduction of low-mass diffraction is very important for the consistency of our approach. Without it, one would need a large value of the triple-Pomeron coupling in order to reproduce the measured single-diffractive cross sections and our first-order treatment of the triple Pomeron would no longer be possible.

In Fig. 5 we present the cross sections for l_c cut soft and m_c cut hard Pomerons (for $n_c=p_c=0$) at two different collision energies in the form of lego plots.

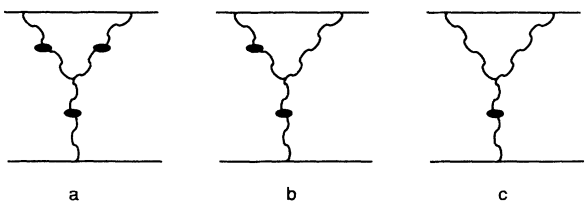

FIG. 3. The three ways to cut the triple-Pomeron graph.

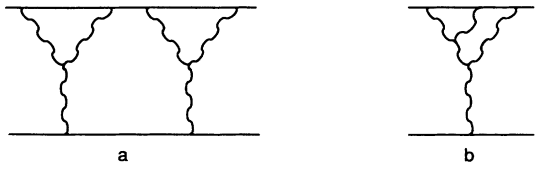

FIG. 4. Higher-order loop graphs containing the triple-Pomeron coupling.

B. Momentum distribution functions of the string ends

We have to sample the constituents at the ends of the different strings. In an event with n_s soft Pomerons we have to sample the $2n_s$ constituents for each of the primary hadrons [valence quark, valence diquark, and $(2n_s-2)/2$ quark-antiquark pairs or gluons which fragment subsequently into quark-antiquark pairs]. This exclusive parton distribution has the form [3]

$$\rho(x_1,\ldots,x_{2_{n_s}})\sim\frac{1}{\sqrt{x_1}}\left[\prod_2^{2n_s-1}\frac{1}{x_i}\right]x_{2n_s}^{1.5}\delta\left[1-\sum_1^{2n_s+n_h}x_i\right]. \tag{2.7}$$

The form of the soft-parton distributions for small x values is obtained by dual Regge arguments. For valence partons

$$\rho(x_q)\sim\frac{1}{x_q^{\alpha_R}},\quad \alpha_R=\tfrac{1}{2},$$
$$f(x_{qq})\sim\frac{1}{x_{qq}^{\alpha_E}},\quad \alpha_E=-1.5, \tag{2.8}$$

where α_R is the leading $(q\bar{q})$ Regge trajectory and α_E the exotic $(qq\bar{q}\bar{q})$ trajectory. The x distribution of soft sea quarks is $f(x)\sim 1/x$ for $x\to 0$.

In an event with n_s soft Pomerons and $n_h(n_h\geq 1)$ hard Pomerons (to be definite we consider as an example the case of hard gluon-gluon scattering) the expression becomes somewhat more complicated. This exclusive parton distribution has the form

$$\rho(x_1,\ldots,x_{2_{n_s}},x_{2n_s+1},\ldots,x_{2n_s+2+n_h})\sim\frac{1}{\sqrt{x_1}}\left[\prod_2^{2n_s+2}\frac{1}{x_1}\right]x_{2n_s}^{1.5}\prod_{2n_s+3}^{2n_s+2+n_h}g(x_i,Q_i)\delta\left[1-\sum_1^{2n_s+2+n_h}x_i\right]. \tag{2.9}$$

The distribution $g(x_i,Q_i)$ are the distribution functions for the x values of partons engaged in the hard scattering.

The triple-Pomeron graph cut such as in Fig. 3(a) and the correspondingly cut loop graph are treated in the same way as two cut soft Pomerons. The triple-Pomeron graph cut such as Fig. 3(b) and the correspondingly cut loop graph are treated in the same way as one cut soft Pomeron. For the triple-Pomeron graph cut such as in Fig. 3(c) (single diffraction) and the corresponding cut of the loop graph (double diffraction) we need a special treatment. The sum of the x values $x_D=x_q+x_{\bar{q}}$ (x_q and $x_{\bar{q}}$ belong to the sea quark and antiquark at the ends of the two diffractive chains) are sampled from a distribution $\approx 1/x_D$ with the condition that the mass M of the diffractive two-chain system satisfies $M^2/s\leq\frac{1}{20}$.

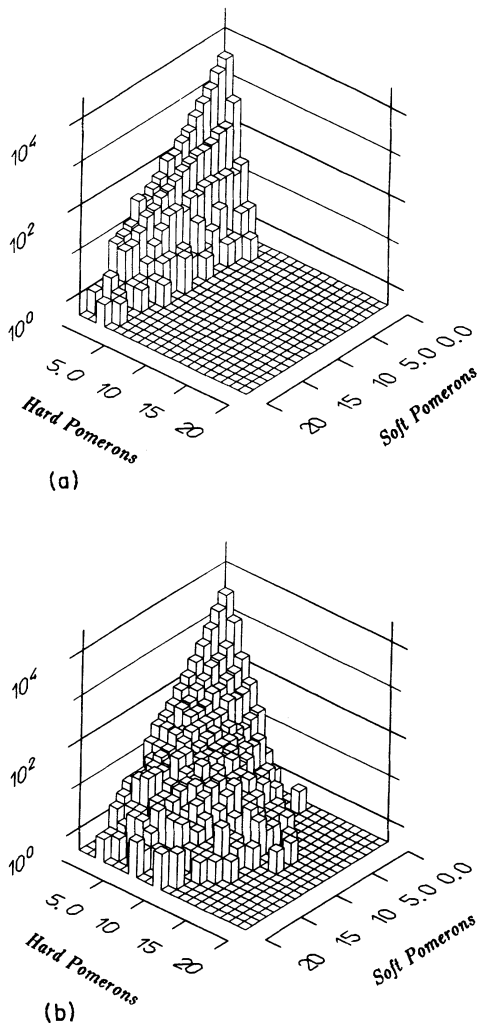

FIG. 5. Cross section given in arbitrary units for the production of given numbers of soft and hard Pomerons in the form of lego plots as obtained from our unitarization scheme: (a) for $\sqrt{s}=1000$ GeV, (b) for $\sqrt{s}=30$ TeV. The comparison of the two graphs makes the dramatic rise of the number of semihard scatterings with rising energy clearly visible.

All data considered in this paper refer to non-single-diffractive events. A comparison of the single-diffraction model with the available data was given in [22].

In the present version of the model we do not use a method sampling exactly from (11), instead we use a rejection method, where the x values of the hard and soft partons are first sampled independently and we reject the

event if the x value remaining for the diquark is inconsistent, that means, if the sum of all x values becomes larger than one. In most configurations the valence diquarks get much larger x values than all other partons and therefore only very few configurations sampled by this approximate method have to be rejected. A method to sample exactly from the exclusive multiparton distribution is also available and gives equivalent results.

C. Intrinsic transverse momenta

The partons at the ends of the hard or semihard chains get transverse momenta $p_\perp \geq p_{\perp\text{thr}}$ as predicted by perturbative QCD. This was described in detail in [14]. It is usual also to give some typically "soft" transverse momenta to the partons at the ends of the chains resulting from the cut soft Pomerons. The subdivision of multiparticle chains into "soft" and "hard" ones is, however, only due to our inability to solve QCD at low $p_\perp$. Therefore, we try to get a continuous transition from soft to hard jets. We introduce for the constituents at the ends of the soft chains a $p_\perp$ distribution, normalized to the average number of soft chains which joins continuously with the hard chain $p_\perp$ distribution at $p_\perp = p_{\perp\text{thr}}$. At small energies, where the hard component is practically absent, the model stays unchanged. At larger energies this continuity requirement gives to the soft chain ends transverse momenta, which are bigger than typical soft ones and which rise with the collision energy. At the energies of the present colliders we get quite similar resulting models with $p_{\perp\text{thr}} = 2$ or 3 GeV/c, if the bare hard cross section is adjusted correspondingly. This means the model is quite independent of the arbitrary value of the transverse momentum cutoff. At collision energies higher than 2 TeV we prefer the cutoff $p_{\perp\text{thr}} = 3$ GeV/c, which allows the transverse momenta of hadrons obtained after the hadronization step to rise with the collision energy up to the energies of the proposed supercolliders. A cutoff of $p_{\perp\text{thr}} = 2$ GeV/c leads to a saturation of the average hadron transverse momenta already at energies of some TeV, which we consider as unphysical. The reason for this saturation in the model is the following. After hadronization we find for the minijet components with parton-transverse-momentum cutoffs $p_{\perp,\text{thr}} = 2$ GeV/c (3 GeV/c) average hadron transverse momenta of about 0.55 GeV/c (0.70 GeV/c). This changes only weakly with the collision energy. At all energies the parton cross section decreases steeply with the transverse momentum above the cutoffs. The average hadron transverse momenta due to the soft component is always smaller. Even with a minijet cross section rising with energy, the average hadron transverse momenta can never become larger than the ones due to the minijet component alone. Also for a cutoff of 3 GeV/c a saturation will occur, however at energies above the TeV energy scale of the proposed super colliders. This saturation is an artifact of the two-component model in its present form; it could be overcome only with a future one-component model giving a unified description of hard and soft chains.

D. Total, inelastic, elastic, and diffractive cross sections

The simultaneous unitarization of the soft and hard hadronic cross sections was first performed in papers by Capella, Tran Thanh Van, and Kwiecinski [11] and Durand and Pi [12]. We use for the soft-input cross section the parameters of the supercritical Pomeron as determined by Capella, Tran Thanh Van, and Kwiecinski [11]; see Appendixes A1 and A2. We use the hard-input cross section as calculated from the QCD parton model using the parton distributions of Martin, Roberts, and Stirling (set 1) [23]; see Appendix A3.

It should be stressed that there is considerable theoretical and experimental uncertainty about this rise of σ_h with the energy. Structure functions such as the ones used here postulate a $1/x$ dependence for gluon- and sea-quark-structure functions at some reference scale ($Q_0^2 \approx 5$ GeV^2) but of course the QCD evolution makes the gluon distribution much steeper of larger Q^2 values. At the x values of 10^{-4} which become important for the production of minijets in the energy region of tens of TeV, the structure functions cannot be determined experimentally at present accelerator energies and there is presently no practical method available which would permit to calculate the structure functions from QCD. It has been argued that the x dependence of the structure functions at these small x values indeed differ from x^{-1}. Collins [24] presented arguments for a $x^{-1.5}$ behavior.

During the last year new improved fits of the structure functions to experimental data became available [25]. However, the uncertainty regarding the behavior at small x values remains. Kwiecinski *et al.* [26] study parton distributions with the singular $x^{-1.5}$ behavior of the gluon and sea-quark distributions. They find significant QCD shadowing corrections [44,45] for $x < 10^{-3}$ and show that even the production of heavy particles such as the Z and W gauge bosons in 10-TeV energy region cannot be predicted reliably at present. We plan in a future paper to study the implications of the different structure functions [25,26] for the minijet component in our model.

In Figs. 6 and 7 we compare cross sections according

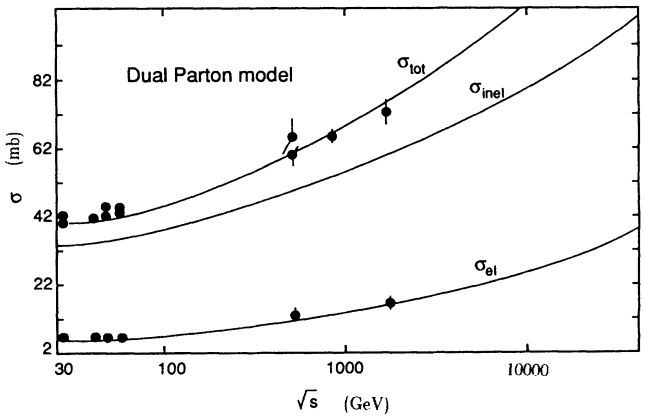

FIG. 6. Comparison of the total cross section σ_{tot} and the elastic cross section σ_{el} as calculated within the model with experimental data [27]–[34].

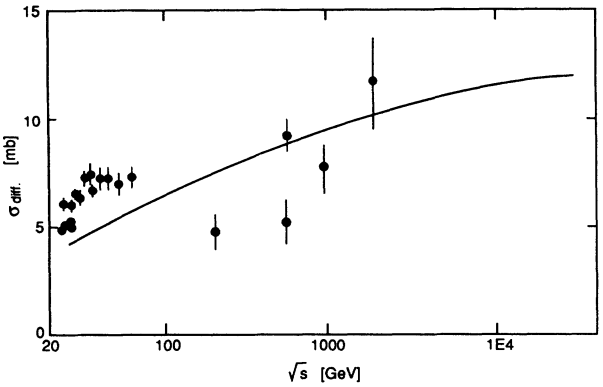

FIG. 7. Comparison of the single-diffractive cross section σ_{SD} as calculated from the model with experimental data [35]–[43].

to our unitarization scheme with data in the energy region from the CERN ISR to the Fermilab collider.

In Fig. 6 we compare the total cross sections and find a rather good agreement with the observed rise with energy. It is, however, obvious that at the highest energies an even better agreement might have been possible had we performed a new fit to the data to adjust the parameters of the supercritical Pomeron (recall, that we use the parameters determined in the fit performed in 1987 [11]). In the same figure, we plot also the calculated inelastic cross section σ_{inel} and compare the elastic cross section σ_{el} in the same energy region with data. The agreement is reasonable.

In Fig. 7 we compare the single-diffractive cross section σ_{SD} with data; this is the sum of the high-mass single-diffractive cross section σ_{HMSD} and the low-mass single-diffractive cross section σ_{LMSD}. The agreement is satisfactory. No attempt has been made to get a precise description of the low-energy region.

We would like to stress that the fit of the model to these cross sections fixes already the essential free input parameters in the model, these are the parameters of the soft, supercritical Pomeron, and the parameter λ entering the two-channel eikonal model; see Appendix B2. We find the optimum value of this parameter to be $\lambda=0.6$ and we shall use this value always throughout this paper.

III. RESULTS

In this section we present results as obtained from the Monte Carlo event generator DTUJET 90 [19]. The transverse-momentum cutoff $p_{\perp,\min}$ was set to 3 GeV/c and the hard scale was $Q^2=p_\perp^2/4$. For the minijets we have not included initial- and final-state bremsstrahlung effects to the hard scattered partons. This will be done for events with higher transverse momentum. For the hadronization of chains, i.e., the transition of partons to hadrons we use the independent-fragmentation chain code BAMJET [46] and the decay of resonances is handled by the code DECAY [47].

A. The rise of the rapidity plateau

In Fig. 8 we present the central rapidity and pseudorapidity plateau of all charged particles as function of the center-of-mass energy $\sqrt{s}$ in the region between $\sqrt{s}=20$ GeV and 40 TeV. Both the rapidity and pseudorapidity plateau rise approximately like log$s$. The rise of the pseudorapidity plateau has been measured at energies up to $\sqrt{s}=1.8$ TeV; in this region the model agrees very well with the data.

In Fig. 9 we present rapidity and pseudorapidity distributions of charged particles at 0.2, 0.54, 0.9, 1.8, 16, and 40 TeV. The pseudorapidity distributions at $\sqrt{s}=0.2$–0.9 TeV are compared with the data from the UA5 Collaboration [48]. The agreement is very good in the central region but the model tends to overestimate the data in the fragmentation region. The extrapolation to the supercollider energies of 16 and 40 TeV seems to be smooth, since, as we have seen in Fig. 8, the plateau continues to rise logarithmically with the same slope as found experimentally. Nevertheless, the calculation corresponds only to minijets according to one particular parametrization of the structure functions. If the structure functions down to x values of $x=10^{-4}$ behave differently, a threshold could be reached between 2 and 40 TeV with a steeper slope of the rising plateau.

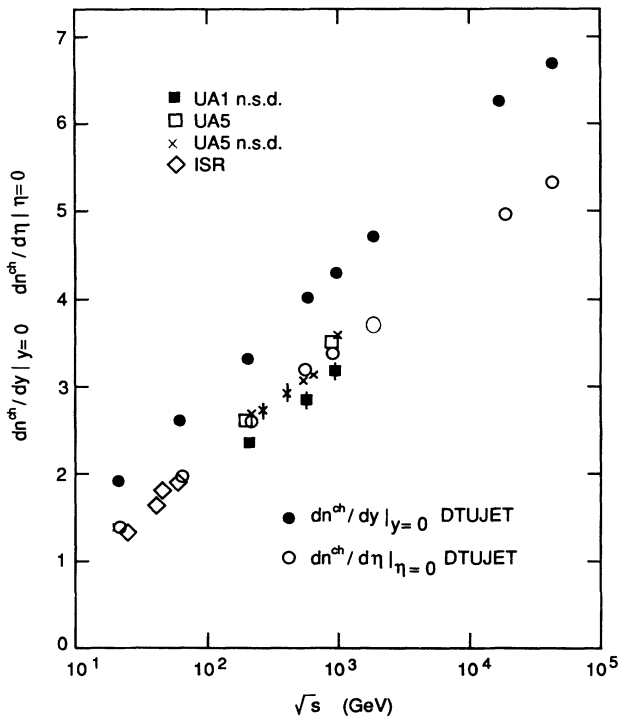

FIG. 8. The central rapidity and pseudorapidity plateau of all charged particles as function of the c.m.-system energy. The rise of the pseudorapidity density is compared to data [48],[49],[52],[53].

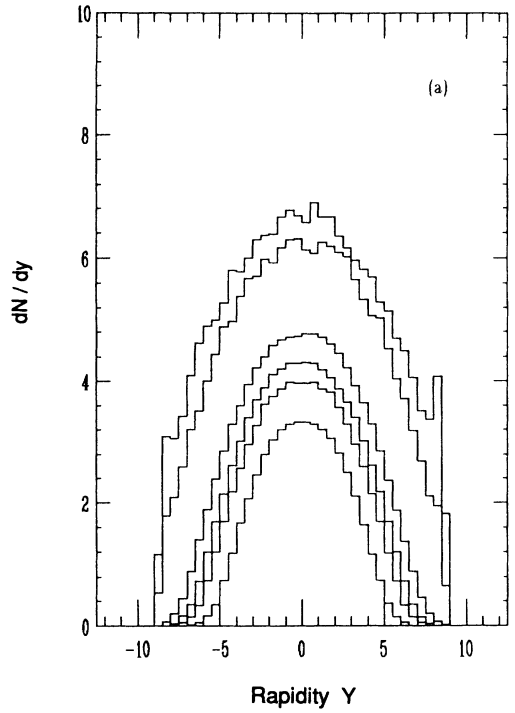

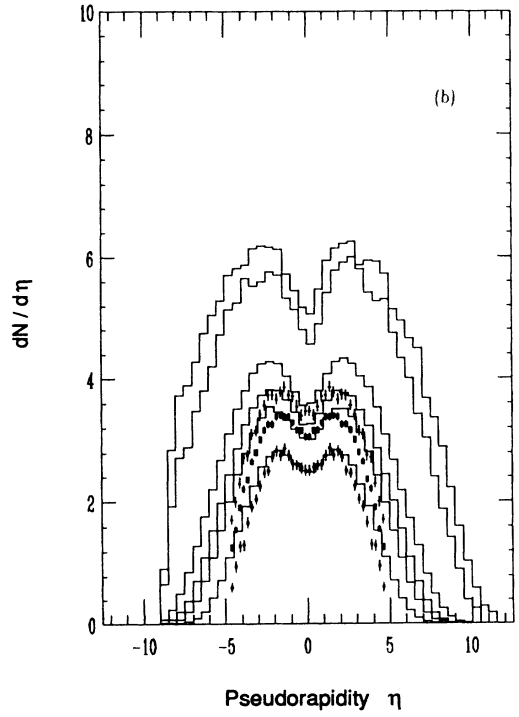

FIG. 9. (a) Rapidity and (b) pseudorapidity distribution of charged particles at 0.2, 0.54, 0.9, 1.8, 16, and 40 TeV. The pseudorapidity distributions at 0.2–0.9 TeV are compared with data from the UA5 Collaboration [48].

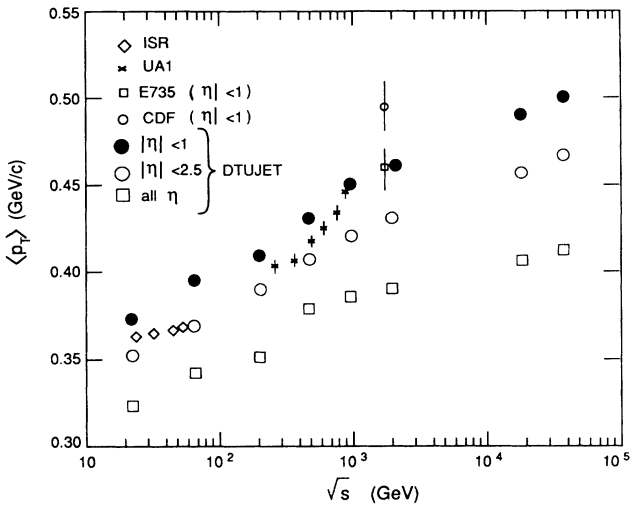

FIG. 10. Rise of average transverse momenta of charged particles in the total pseudorapidity region and in restricted regions $|\eta| \leq 2.5$ and $\eta| \leq 1$. The model predictions are compared to data [54],[55].

B. The rise of average transverse momenta

Transverse-momentum distributions of charged particles according to the model were computed by Hahn and Ranft [14]. The correlation between the central multiplicity and the average transverse momenta of pions, kaons, and antinucleons was already compared to data by Bopp *et al.* [15]. Here we present in Fig. 10 the rise of the average transverse momentum of charged particles in different rapidity windows as function of the collision energy. The average transverse-momenta rise proportional to log$s$. The agreement with data is good in the energy region of past and present colliders.

The extrapolation provided by the model seems to be safe, since the average transverse momenta continue to rise logarithmically with a slope which corresponds to the slope of the experimental data. But again, if the structure functions down to $x = 10^{-4}$ behave differently from the present extrapolations, a threshold connected with a change of this slope could occur in the TeV energy range.

In Table I we present material which indicates that there would be room for a minijet-related threshold in the rapidity plateau and the average $p_\perp$ in the TeV energy region. The three main components of the present model

TABLE I. Multiplicities, average transverse momenta, and rapidity plateaus separately according to the three main components of the model: soft valence chains (sv), soft sea chain (ss), and hard chains (h).

$\sqrt{s}$		$p_{\perp,sv}$			$p_{\perp,ss}$				$p_{\perp,h}$	
(TeV)	n_{sv}	(GeV/c)	$\frac{dn}{dy_{sv}}$	n_{ss}	(GeV/c)	$\frac{dn}{dy_{ss}}$	n_h	(GeV/c)	$\frac{dn}{dy_h}$
0.9	49.3	0.35	2.6	18.1	0.42	1.5	1.64	0.70	0.1
1.8	58.5	0.34	2.7	22.7	0.43	1.7	2.86	0.69	0.1
16.0	88.5	0.36	3.0	42.9	0.43	2.5	10.2	0.68	0.6
40.0	98.0	0.37	3.0	54.0	0.43	2.8	16.2	0.69	0.9

are soft valence chains, soft sea chains, and hard chains (minijets). In Table I we give for energies between 200 GeV and 40 TeV separately for the three mechanisms the average multiplicities, average transverse momenta, and rapidity plateaus. Clearly, in this energy range the soft valence chains still dominate and the minijets are still rather unimportant. The situation could be changed strongly, if the gluon structure function and correspondingly the minijet cross section at large $\sqrt{s}$ would increase significantly, say by a factor of 5 or so. Such a rise is likely to occur with the structure functions recently proposed by Kwiecinski *et al.* [26].

C. Transverse-energy distributions

Transverse-energy cross sections $d\sigma/d\sum E_\perp$ were measured by the UA1 Collaboration [49] in the pseudorapidity range $|\eta| \leq 6$ at energies between 0.2 and 0.9 TeV. In Fig. 11 we compare the transverse-energy cross section with the cross section calculated in our model. We find at 0.2 and at 0.54 TeV a rather good agreement with the data. At 0.9 TeV the tail of the experimental data is well above the calculated histogram; there is no obvious reason which could be responsible for this disagreement.

D. Multiplicity distributions

It has been pointed out repeatedly [3,5] that the dual parton model violates KNO scaling. This was also found in Monte Carlo calculations [6,7]. A non-KNO-scaling behavior of this type was also found by the UA5 Collaboration [42].

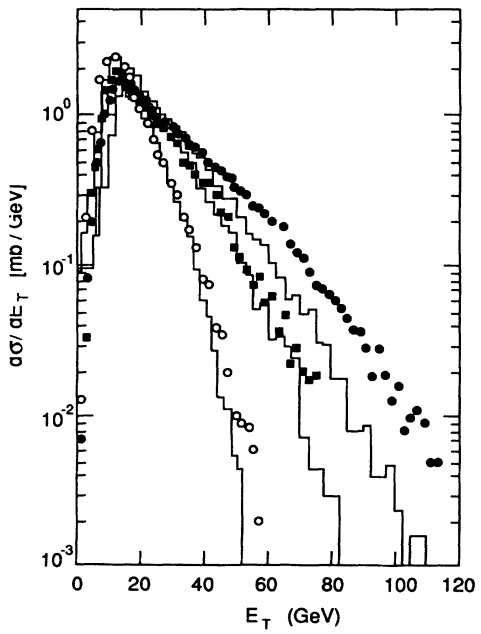

FIG. 11. Comparison of calculated transverse-energy distributions with data from the UA1 Collaboration [49].

In Fig. 12 we compare the multiplicity distributions measured by the UA1 Collaboration [49] for $|\eta| \leq 2.5$ at 200, 500, and 900 GeV with the calculated multiplicity distributions. We find a reasonable agreement as well of the position of the maximum as of the general shape between the measured and calculated multiplicity distributions.

In Fig. 13 we compare the multiplicity distributions measured by the UA5 Collaboration [50] for $|\eta| \leq 5$ at 200 and 900 GeV with the calculated non-single-diffractive multiplicity distributions. At the high-multiplicity tails of the distributions we find a reasonable agreement. However, there is a noticeable disagreement regarding the positions of the maxima of the distributions. The maxima of the calculated distributions are at higher values of the multiplicity n. The disagreement can be attributed to low-multiplicity events. We would however like to point out that in [13], taking the acceptance of the experiment properly into account, a better fit to the data was obtained with a DPM Monte Carlo program similar to ours.

IV. SUMMARY

Our model was already briefly described in a first paper [15]. The present paper gives the full account of the model and compares the Monte Carlo results with further experimental data. Here we study for the first time multiparticle production in the complete model including both high-mass and low-mass diffraction.

Particle production in the two-component dual parton model is highly constrained by (i) the measured cross sections σ_{tot}, σ_{inel}, σ_{el}, and σ_{diffr}, (ii) the unitarization scheme, which predicts the exclusive multi-Pomeron cross sections, and (iii) the QCD parton model, which is used to calculate the hard-input cross sections σ_h.

Even without a new fit to the total, elastic, and inelastic cross sections (we use still the parametrization of the Pomeron obtained in the fit by Capella, Tran Thanh Van, and Kwiecinski [11]), we get a good description of the total, inelastic, elastic, and single-diffractive cross sections.

The model is found to be consistent with a wealth of data in the collider energy range. The Monte Carlo model contains high-mass single diffraction and double diffraction. However, single diffraction has been excluded from the comparisons with most data, where single diffraction is also excluded.

We find good agreement with the following features of multiparticle production.

(1) The rise of the rapidity plateau with the collision energy.

(2) The rise of average transverse momenta and the tail of the transverse-momentum distribution with the collision energy [14].

(3) The violation of KNO scaling of the multiplicity distribution and the shape of the multiplicity distribution.

(4) The correlation of average transverse momenta with multiplicity [15].

(5) The pedestal effect in the low-$p_\perp$ events under the hard jets [14].

(6) Forward-backward correlations [15].

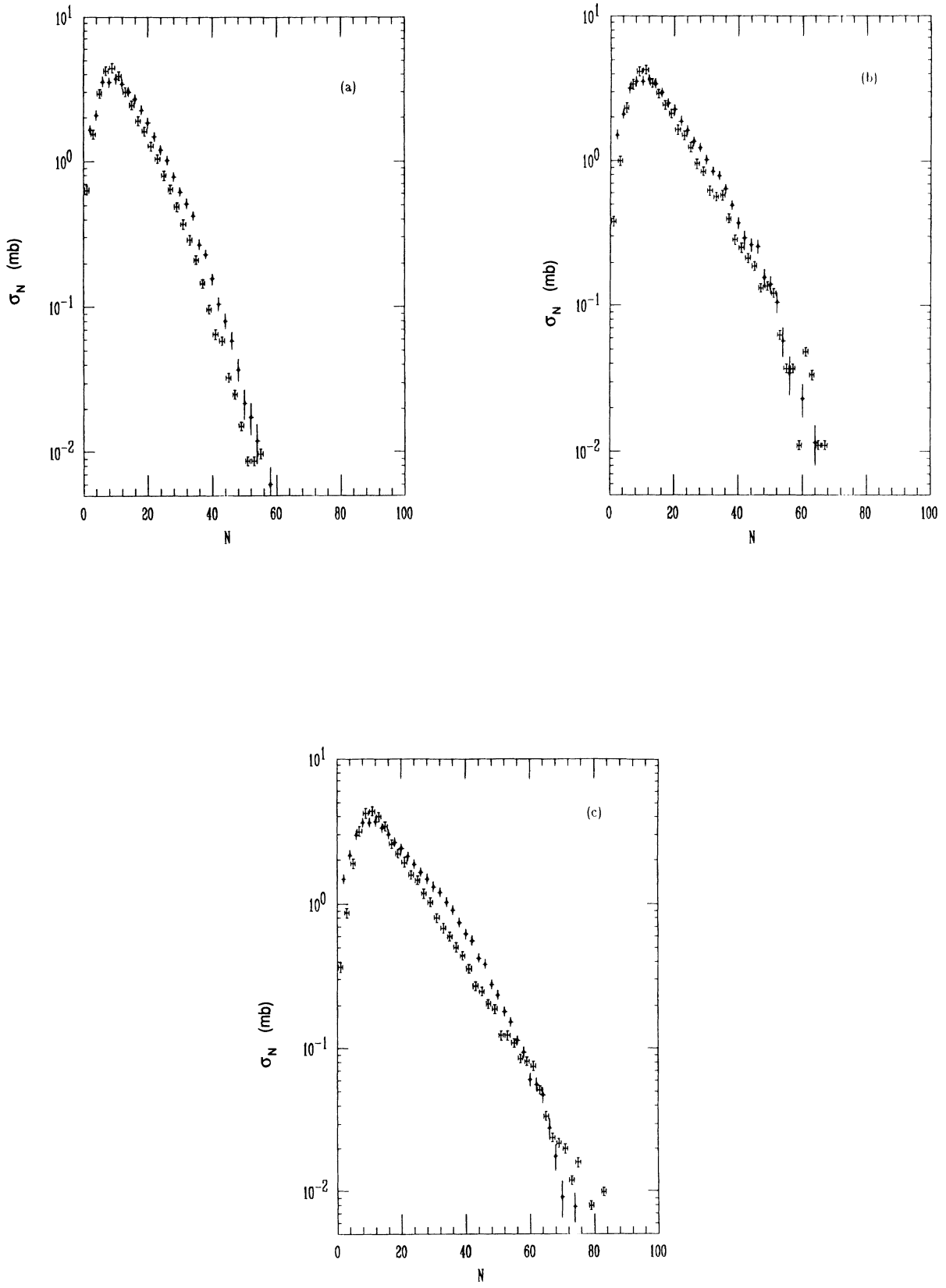

FIG. 12. Comparison of the calculated multiplicity distributions for $|\eta| \leq 2.5$ with data from the UA1 Collaboration [49] (a) for 200 GeV, (b) for 500 GeV, (c) for 900 GeV. The experimental data (but not the model results) are given by symbols with error bars.

(7) Transverse-energy distributions.

(8) Rapidity and pseudorapidity distributions.

(9) The rise of factorial moments [15]. The first comparison of the model with intermittency phenomena is encouraging, but a quantitative agreement is not yet found.

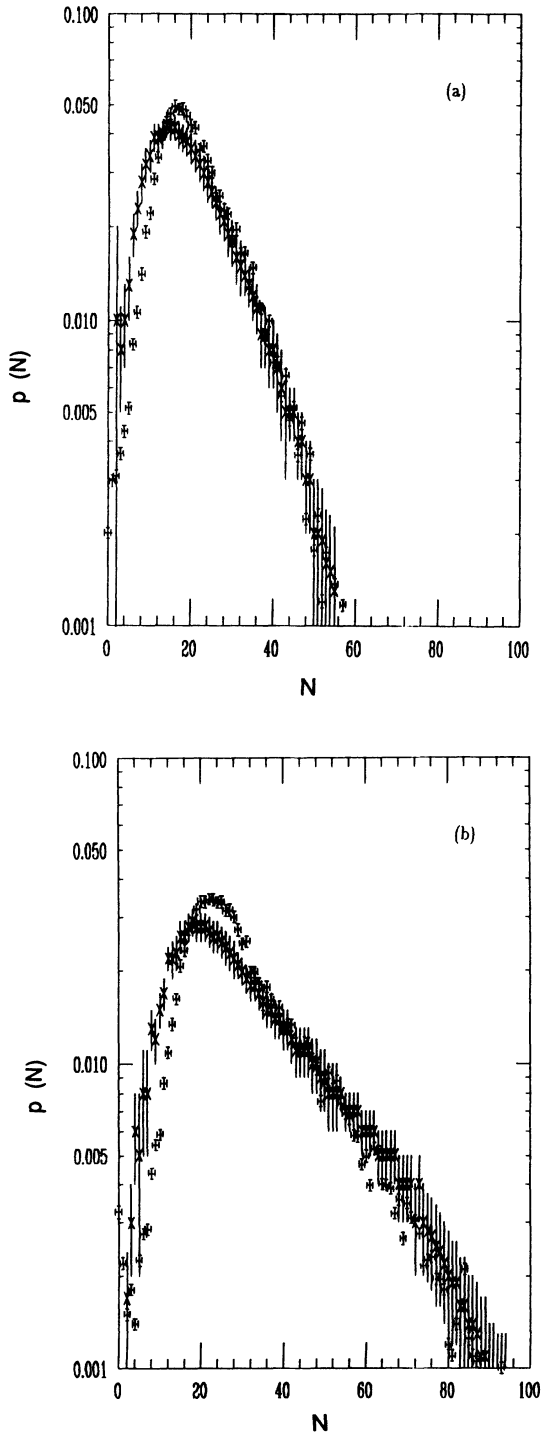

FIG. 13. Comparison of calculated multiplicity distributions for $|\eta| \leq 5$ with data from the UA5 Collaboration [50] (a) for 200 GeV, (b) for 900 GeV. The experimental data (but not the model results) are given by symbols with error bars.

Our aim was more to find an overall agreement with most of the features of multihadron production known from experiment rather than a detailed fit to a single experiment using all necessary corrections and acceptances of the experiment.

The most important lines for a further improvement of the model could be to find theoretical guidelines to constrain the string fragmentation in the model and to work towards a unified description of the hard and soft components of the model. Also the implications of nonconventional gluon distributions on the minijet component at the energies of future supercolliders will be studied.

ACKNOWLEDGMENTS

Two of the authors (J.R. and F.W.B.) thank Professor A. Capella, Professor K. Chadan, and Professor J. Tran Thanh Van for the invitation to Laboratoire de Physique Theorique et Particules Elémentaires, Université de Paris-Sud (L.P.T.H.E.), Orsay. One of the authors (J.R.) thanks Dr. K. Goebel and Dr. G. R. Stevenson for invitations to CERN, where part of the calculations reported here were done.

APPENDIX A: INPUT CROSS SECTIONS FOR THE DPM UNITARIZATION SCHEME

We include four different cross sections into the unitarization scheme. These are the soft hadronic cross sections, the semihard or hard cross section, the single-diffractive or triple-Pomeron cross section, and the double-diffractive or loop cross section.

1. The soft input cross section σ_s

The soft-input cross section σ_s is parametrized according to the supercritical Pomeron with parameters as determined by Capella, Tran Thanh Van, and Kwiecinski [11]:

$$\sigma_s = g^2 s^{\Delta} \tag{A1}$$

with

$$g^2 = 40.8 \text{ mb} \tag{A2}$$

and the Pomeron intercept

$$\Delta = \alpha(0) - 1 \, . \tag{A3}$$

The Pomeron trajectory is given by

$$\alpha(t) = \alpha(0) + \alpha' t \tag{A4}$$

with

$$\alpha(0) = 1.076 \text{ and } \alpha' = 0.24 \text{ GeV}^{-2} \, . \tag{A5}$$

2. The single-diffractive and double-diffractive input cross sections

The single-diffractive input cross section σ_{SD} is obtained by integrating the triple-Pomeron cross section ($\approx \exp b_{SD} t / M^2$) over t and in the range $5 \text{ GeV}^2 \leq M^2 \leq s/20$ over M^2:

$$\sigma_{TP}=\sigma_{SD}=\frac{2}{16\pi}\frac{g^3\Gamma}{b_{SD}}\ln\frac{s}{100\ \text{GeV}^2}\ . \tag{A6}$$

The double-diffractive cross section is obtained by integrating a distribution [$\approx\exp(b_{DD}t/M_1^2M_2^2)$] over both masses

$$\sigma_L=\sigma_{DD}=\frac{1}{16\pi}\frac{g^2\Gamma^2}{2b_{DD}}\left[\ln^2\frac{s}{400\ \text{GeV}^2}+\ln^2\frac{25}{5}-2\ln\frac{5}{20}\right] \tag{A7}$$

with the slopes in σ_{SD},

$$b_{SD}=b_{SD}^0+2\alpha'\ln s\ , \tag{A8}$$

$$b_{SD}^0=1.372\ \text{mb}=3.7\ \text{GeV}^{-2},\quad \alpha'=0.0925\ \text{mb}=0.24\ \text{GeV}^{-2}\ , \tag{A9}$$

and

$$\Gamma=0.42\ \text{mb}^{1/2} \tag{A10}$$

and the slope in σ_{DD}

$$b_{DD}=2\alpha'\ln s\ . \tag{A11}$$

3. Hard constituent scattering cross sections

The calculation and sampling of hard constituent scattering cross sections within our model was described in detail in [14]. We use in the calculation the parton-parton scattering cross sections as obtained by Combridge, Kripfganz, and Ranft [51] in lowest-order QCD perturbation theory and the quark and gluon distribution functions in the parametrization of Martin, Roberts, and Sterling (set 1) [23]. The results are essentially unchanged, if other popular parametrizations for the structure functions are used. In order to remain in the region where the QCD perturbation theory is valid, we use for the minijet component a low $p_\perp$ cutoff $p_{\perp\text{thr}}$. The outcome of the model should not depend on the exact value of this cutoff; we use values $p_{\perp\text{thr}}=2$ GeV/c and $p_{\perp\text{thr}}=3$ GeV/c. In the energy region of hadron colliders up to $\sqrt{s}=1$ or 2 TeV the results are indeed nearly independent on the cutoff. At higher energies, we prefer the higher value of the cutoff; see the end of Sec. II A.

In Table II we give calculated values of the hard cross sections σ_h for the cutoffs of 2 and 3 GeV/c. This table can be used to determine σ_h at other energies by interpolation.

APPENDIX B: UNITARIZATION OF THE CROSS SECTIONS

1. Model with soft and hard cross sections and high-mass diffraction

We start from input cross sections in the impact parameter representation (eikonal) and describe first a model with only high-mass diffraction represented by the triple-pomeron graph (single diffraction) and a loop graph (double diffraction). We introduce the soft cross section

$$\chi_s(B,s)=\frac{\sigma_s}{8\pi b_s}\exp\left[-\frac{B^2}{4b_s}\right], \tag{B1}$$

the hard cross section

$$\chi_h(B,s)=\frac{\sigma_h}{8\pi b_h}\exp\left[-\frac{B^2}{4b_h}\right], \tag{B2}$$

the triple-Pomeron cross section

$$\chi_{TP}(B,s)=\frac{\sigma_{TP}}{8\pi b_{TP}}\exp\left[-\frac{B^2}{4b_{TP}}\right], \tag{B3}$$

and the loop cross section

$$\chi_L(B,s)=\frac{\sigma_L}{8\pi b_L}\exp\left[-\frac{B^2}{4b_L}\right]. \tag{B4}$$

We use the slopes $b=3.52$ GeV^2 and $b_h=b$, $b_s=b_{TP}=b_L=b+\alpha'\ln(s/1\ \text{GeV}^2)$. The normalization of these cross sections is given by

$$\int 2\chi_i(B,s)d^2B=\sigma_i\ . \tag{B5}$$

In Fig. 2 we give the Pomeron-exchange graphs, which correspond to these cross sections.

Let us now consider the exclusive cross sections with l_c cut soft Pomerons, m_c cut hard Pomerons, m_c cut triple-Pomeron graphs, and p_c cut loop graphs. These are the cross sections, which we need for the construction of inelastic events in the dual parton model. In the eikonal model we have

TABLE II. Cross sections for the hard scattering of constituents with lower $p_\perp$ cutoffs $p_{\perp\text{thr}}=2$ and 3 GeV/c calculated with parton distributions according to Martin, Roberts, and Stirling [23]; set 1 with $\Lambda=0.107$ GeV.

$\sqrt{s}$ (TeV)	σ_h (mb) $p_{\perp\text{thr}}=2$ GeV/c	σ_h (mb) $p_{\perp\text{thr}}=3$ GeV/c
0.005	1.1×10^{-8}	
0.01	1.4×10^{-3}	7×10^{-6}
0.02	0.099	4.7×10^{-3}
0.035	0.58	0.058
0.053	1.48	0.196
0.15	4.22	0.73
0.2	9.76	2.02
0.35	16.6	3.79
0.54	23.7	5.72
1.0	36.7	9.53
2.0	56.4	15.7
5.0	91.5	27.8
10.0	126.3	40.9
20.0	168.3	57.8
40.0	219.3	79.3
100.0	301.0	116.
200.0	375.0	158.

$$\sigma(l_c,m_c,n_c,p_c,B,s)=\frac{(2\chi_s)^{l_c}}{l_c!}\frac{(2\chi_h)^{m_c}}{m_c!}\frac{(-2\chi_{\rm TP})^{n_c}}{n_c!}\frac{(-2\chi_L)^{p_c}}{p_c!}e^{-2\chi(B,s)} \tag{B6}$$

with

$$\chi(B,s)=\chi_s(B,s)+\chi_h(B,s)-\chi_{\rm TP}(B,s)-\chi_L(B,s)\ . \tag{B7}$$

We obtain the unitarized hadronic cross sections as follows. The inelastic cross section

$$\sigma_{\rm inel}=\int d^2B\sum_{l_c+m_c+n_c+p_c\geq 1}\sigma(l_c,m_c,n_c,p_c,B,s)$$
$$=2\pi\int_0^\infty B\,dB(1-e^{-2\chi(B,s)})\ , \tag{B8}$$

the inelastic cross section with at least one hard or semihard scattering,

$$\sigma_{h,\rm inel}=\int d^2B\sum_{m_c\geq 1}\sigma(l_c,m_c,n_c,p_c,B,s)$$
$$=2\pi\int_0^\infty B\,dB(1-e^{-2\chi_h(B,s)})\ , \tag{B9}$$

the single-diffractive cross section,

$$\sigma_{\rm SD}=\int d^2B\sum_{n_c\geq 1}\sigma(0,0,n_c,0,B,s)$$
$$=4\pi\int_0^\infty B\,dB(e^{\chi_{\rm TP}(B,s)}-1)e^{-2\chi(B,s)}\ . \tag{B10}$$

The total cross section is given by

$$\sigma_{\rm tot}=4\pi\int_0^\infty B\,dB(1-e^{-\chi(B,s)})\ . \tag{B11}$$

Notice that this last formula is only approximate, since we have neglected the real parts of the eikonal.

2. Model with high-mass diffraction and low-mass diffraction introduced via a two-channel eikonal formalism

Besides the high-mass diffraction introduced above we introduce in addition low-mass diffraction via a two-channel eikonal formalism. We introduce a new coupling λ, which appears in the three graphs with the low-mass excitation given in Fig. 14:

$$\text{(a) }\lambda\chi_s(B,s),\quad\text{(b) }\lambda\chi_s(B,s),\quad\text{(c)}\lambda^2\chi_s(B,s)\ . \tag{B12}$$

The result is that each graph with l soft, m hard, n triple-Pomeron, and p loop exchanges has to be modified by a factor

$$X_{l+m+n+p}(\lambda)X_{l+m+2n+p}(\lambda) \tag{B13}$$

with

$$X_i(\lambda)=\tfrac{1}{2}[(1+\lambda)^i+(1-\lambda)^i]\ . \tag{B14}$$

It is to be noted that we have treated approximately all triple-Pomeron contributions to be equal irrespectively whether the two legs of the graph point to the upper or lower line. This approximation is justified, if the triple-Pomeron coupling is so weak, that it is sufficient to treat both the triple-Pomeron graph and the loop graph only to first order. We will comment on this again later.

We calculate (B13) and obtain

$$X_{l+m+n+p}(\lambda)X_{l+m+2n+p}(\lambda)=\tfrac{1}{4}\{(1+\lambda)^{2l+2m+3n+2p}+(1-\lambda)^{2l+2m+3n+2p}+(1-\lambda^2)^{l+m+n+p}[(1+\lambda)^n+(1-\lambda)^n]\}\ . \tag{B15}$$

Therefore we obtain now for the different cross sections in the impact parameter representation the total cross section

$$\sigma_{\rm tot}(B,s)=\tfrac{1}{4}(\sigma_{\rm tot}^{(1)}+\sigma_{\rm tot}^{(2)}+\sigma_{\rm tot}^{(3)}+\sigma_{\rm tot}^{(4)}) \tag{B16}$$

with

$$\sigma_{\rm tot}^{(i)}=2(1-e^{-\chi^i(B,s)}) \tag{B17}$$

and

$$\chi_i(B,s)=\chi_s^{(i)}+\chi_h^{(i)}-\chi_{\rm TP}^{(i)}-\chi_L^{(i)}\ . \tag{B18}$$

For $i=s,h$, or l we have

$$\chi_i^{(1)}=(1+\lambda)^2\chi_i(B,s)\ , \tag{B19}$$
$$\chi_i^{(2)}=(1-\lambda)^2\chi_i(B,s)\ , \tag{B20}$$
$$\chi_i^{(3)}=\chi_i^{(4)}=(1-\lambda^2)\chi_i(B,s)\ , \tag{B21}$$
$$\chi_{\rm TP}^{(1)}=(1+\lambda)^3\chi_{\rm TP}(B,s)\ , \tag{B22}$$
$$\chi_{\rm TP}^{(2)}=(1-\lambda)^3\chi_{\rm TP}(B,s)\ , \tag{B23}$$
$$\chi_{\rm TP}^{(3)}=(1-\lambda^2)(1+\lambda)\chi_{\rm TP}(B,s)\ , \tag{B24}$$
$$\chi_{\rm TP}^{(4)}=(1-\lambda^2)(1-\lambda)\chi_{\rm TP}(B,s)\ . \tag{B25}$$

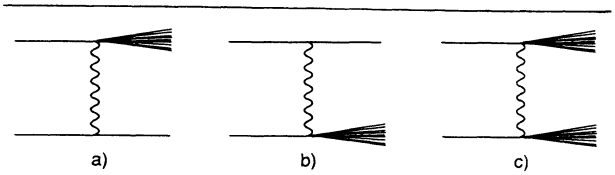

FIG. 14. Low-mass diffractive states introduced in the two-channel eikonal formalism.

The inelastic cross section without low-mass single and double diffraction,

$$\tilde\sigma_{\rm inel}=\sigma_{\rm inel}-\sigma_{\rm LMSD}-\sigma_{\rm LMDD}\ , \tag{B26}$$

is obtained from

$$\tilde\sigma_{\rm inel}(B,s)=\tfrac{1}{4}(\tilde\sigma_{\rm inel}^{(1)}+\tilde\sigma_{\rm inel}^{(2)}+\tilde\sigma_{\rm inel}^{(3)}+\tilde\sigma_{\rm inel}^{(4)}) \tag{B27}$$

with

$$\tilde{\sigma}_{\text{inel}}^{(i)}=(1-e^{-2\chi^{(i)}(B,s)}) . \tag{B28}$$

The elastic cross section is obtained from

$$\sigma_{\text{el}}(B,s)=\tfrac{1}{4}[\sigma_{\text{tot}}(B,s)]^2 . \tag{B29}$$

The low-mass single-diffractive cross section is obtained from

$$\sigma_{\text{LMSD}}(B,s)=\tfrac{1}{8}(e^{-\chi^{(1)}}-e^{-\chi^{(2)}})^2 . \tag{B30}$$

The low-mass double-diffractive cross section is obtained from

$$\sigma_{\text{LMDD}}(B,s)=\tfrac{1}{16}(e^{-\chi^{(1)}}+e^{-\chi^{(2)}}-e^{-\chi^{(3)}}-e^{-\chi^{(4)}})^2 . \tag{B31}$$

The inelastic cross section with at least one hard scattering is obtained from

$$\sigma_{h,\text{inel}}(B,s)=1-\tfrac{1}{4}(e^{-2\chi_h^{(1)}}+e^{-2\chi_h^{(2)}}+2e^{-2\chi_h^{(3)}}) . \tag{B32}$$

Finally, we write the exclusive cross section for l_c cut soft Pomerons, m_c cut hard Pomerons, n_c cut triple-Pomeron graphs, and p_c cut loop graphs:

$$\sigma^{(i)}(l_c,m_c,n_c,p_c,B,s)=\frac{(2\chi_s^{(i)})^{l_c}}{l_c!}\frac{(2\chi_h^{(i)})^{m_c}}{m_c!}\frac{(-2\chi_{\text{TP}}^{(i)})^{n_c}}{n_c!}\frac{(-2\chi_L^{(i)})^{p_c}}{p_c!}e^{-2\chi^{(i)}(B,s)} , \tag{B33}$$

$$\sigma(l_c,m_c,n_c,p_c,B,s)=\tfrac{1}{4}[\sigma^{(1)}(l_c,m_c,n_c,p_c,B,s)+\sigma^{(2)}(l_c,m_c,n_c,p_c,B,s)+\sigma^{(3)}(l_c,m_c,n_c,p_c,B,s)+\sigma^{(4)}(l_c,m_c,n_c,p_c,B,s)] . \tag{B34}$$

The high-mass single-diffractive cross section is obtained as

$$\tilde{\sigma}_{\text{HMSD}}(B,s)=\sum_{n_c\geq 1}\sigma_{0,0,n_c,0}=\tfrac{1}{4}\sum_{i=1}^{4}\tilde{\sigma}_{\text{HMSD}}^{(i)} \tag{B35}$$

with

$$\tilde{\sigma}_{\text{HMDS}}^{(i)}=[\exp(\chi_{\text{TP}}^{(i)})-1]\exp(-2\chi^{(i)}) . \tag{B36}$$

It is to be noted that this is in reality $\tilde{\sigma}_{\text{HMSD}}=\sigma_{\text{HMSD}}+\sigma_{\text{HMLMDD}}$ (high-mass–low-mass double diffraction).

The high-mass double-diffractive cross section becomes

$$\sigma_{\text{HMDD}}(B,s)=\sum_{p_c\geq 1}\sigma_{0,0,0,p_c}=\tfrac{1}{4}\sum_{i=1}^{4}\sigma_{\text{HMDD}}^{(i)} \tag{B37}$$

with

$$\sigma_{\text{HMDD}}^{(i)}=[\exp(\chi_L^{(i)})-1]\exp(-2\chi^{(i)}) . \tag{B38}$$

[1] R. P. Feynman, in *Particle Physics,* Proceedings of the Conference, Irvine, California, 1971, edited by M. Bander, G. L. Shaw, and D. Y. Wong, AIP Conf. Proc. No. 6 (AIP, New York, 1972).

[2] L. N. Lipatov, in *Perturbative QCD,* edited by A. H. Mueller (World Scientific, Singapore, 1989).

[3] A. Capella, U. Sukhatme, Chung I Tan, and J. Tran Thanh Van, Phys. Lett. **81B**, 68 (1979); A. Capella and J. Tran Thanh Van, Z. Phys. C **10**, 249 (1981); Phys. Lett. **114B**, 450 (1982).

[4] P. Aurenche and F. W. Bopp, Z. Phys. C **13**, 205 (1982); Phys. Lett. **114B**, 363 (1982).

[5] A. B. Kaidalov, Phys. Lett. **116B**, 459 (1982); A. B. Kaidalov and K. A. Ter-Martirosyan, *ibid.* **117B**, 247 (1982).

[6] J. Ranft, P. Aurenche, and F. W. Bopp, Z. Phys. C **26**, 279 (1984); P. Aurenche, F. W. Bopp, and J. Ranft, *ibid.* **23**, 67 (1984).

[7] P. Aurenche, F. W. Bopp, and J. Ranft, Phys. Rev. D **33**, 1867 (1986).

[8] Z. Koba, H. B. Nielsen, and P. Olesen, Nucl. Phys. **C29**, 201 (1972).

[9] UA1 Collaboration, G. Arnison *et al.*, Phys. Lett. **118B**, 167 (1982).

[10] UA1 Collaboration, C.-E. Wulz, CERN Report No. CERN-EP/82-84, 1987 (unpublished).

[11] A. Capella, J. Tran Thanh Van, and J. Kwiecinski, Phys. Rev. Lett. **58**, 2015 (1987).

[12] J. Durand and H. Pi, Phys. Rev. Lett. **58**, 303 (1987).

[13] J. Ranft, P. Aurenche, F. W. Bopp, A. Capella, K. Hahn, J. Kwiecinski, M. Maire, and J. Tran Thanh Van, SSC Report No. SSC-149, 1987 (unpublished).

[14] K. Hahn and J. Ranft and Phys. Rev. D **41**, 1463 (1990).

[15] F. W. Bopp, A. Capella, J. Ranft, and J. Tran Thanh Van, Z. Phys. C **51**, 99 (1991).

[16] P. Aurenche and S. Voloshin, Z. Phys. C **49**, 343 (1991).

[17] J. Ranft, Report No. SSC-150, 1987 (unpublished).

[18] J. Ranft and K. Hahn, CERN Report No. TIS-RP/218, 1988 (unpublished).

[19] P. Aurenche, F. W. Bopp, K. Hahn, M. Maire, and J. Ranft (unpublished).

[20] V. A. Abramovski, V. N. Gribov, and O. V. Kancheli, Yad. Fiz. **18**, 595 (1973) [Sov. J. Nucl. Phys. **18**, 308 (1974)].

[21] A. B. Kaidalov, L. A. Ponomarev, and K. A. Ter-Martyrosian, Yad. Fiz. **44**, 722 (1986) [Sov. J. Nucl. Phys. **44**, 468 (1986)].

[22] V. Innocente, A. Capella, A. V. Ramallo, and J. Tran Thanh Van, Phys. Lett. **169B**, 285 (1987); J. Ranft, Z. Phys. C **33**, 517 (1987).

[23] A. D. Martin, R. G. Roberts, and W. J. Stirling, Phys. Rev. D **37**, 1161 (1988).
[24] J. C. Collins, Illinois Tech. Report No. 86-0298, 1986 (unpublished).
[25] P. N. Harriman, A. D. Martin, W. J. Stirling, and R. G. Roberts, Phys. Rev. D **42**, 798 (1990).
[26] J. Kwiecinski, A. D. Martin, W. J. Stirling, and R. G. Roberts, Phys. Rev. D **42**, 3645 (1990).
[27] E-710 Collaboration, N. A. Amos *et al.*, Cornell Report No. CLNS 981, 1990 (unpublished).
[28] A. S. Caroll *et al.*, Phys. Lett. **61B**, 303 (1976); **80B**, 423 (1979).
[29] N. A. Amos *et al.* Nucl. Phys. **B262**, 689 (1985).
[30] M. Ambrosio *et al.*, Phys. Lett. **115B**, 495 (1982).
[31] D. Bernard *et al.* Phys. Lett. B **198**, 583 (1987).
[32] G. Arnison *et al.*, Phys. Lett. **128B**, 336 (1983).
[33] D. S. Ayers *et al.*, Phys. Rev. D **15**, 3105 (1977).
[34] M. Bozzo *et al.*, Phys. Lett. **147B**, 392 (1984).
[35] J. W. Chapman *et al.*, Phys. Rev. Lett. **32**, 257 (1974).
[36] J. Schamberger *et al.*, Phys. Rev. Lett. **34**, 1121 (1975).
[37] S. Barish *et al.*, Phys. Rev. D **9**, 2689 (1974).
[38] M. G. Albrow *et al.*, Nucl. Phys. **B108**, 1 (1976).
[39] J. C. M. Armitage *et al.*, Nucl. Phys. **B194**, 1365 (1982).
[40] J. Whitmore *et al.*, Phys. Rep. C **10**, 273 (1974).
[41] R. E. Ansorge *et al.*, Z. Phys. C **33**, 175 (1986).
[42] G. J. Alner *et al.*, Phys. Rep. C **154**, 247 (1987).
[43] D. Bernard *et al.*, Phys. Lett. B **186**, 227 (1987).
[44] L. V. Gribov, E. M. Levin, and M. G. Ryskin, Phys. Rep. **100**, 1 (1983).
[45] A. H. Mueller and J. Qiu, Nucl. Phys. **B268**, 427 (1986).
[46] S. Ritter and J. Ranft, Acta Phys. Pol. B **11**, 259 (1980); S. Ritter, Z. Phys. C **6**, 27 (1982); Comput. Phys. Commun. **31**, 393 (1984).
[47] K. Hänssgen and S. Ritter, Comput. Phys. Commun. **31**, 411 (1984).
[48] UA5 Collaboration, G. J. Alner *et al.*, Z. Phys. C **33**, 1 (1986).
[49] UA1 Collaboration, C. Albajar *et al.*, CERN Report No. CERN-EP/89-85 (unpublished).
[50] UA5 Collaboration, R. E. Ansorge *et al.*, Z. Phys. C **43**, 357 (1989).
[51] B. L. Combridge, J. Kripfganz, and J. Ranft, Phys. Lett. **70B**, 234 (1977).
[52] W. Thomé *et al.*, Nucl. Phys. **B129**, 365 (1977).
[53] K. Alpgard *et al.*, Phys. Lett. **112B**, 183 (1982).
[54] CDF Collaboration, F. Abe *et al.*, Phys. Rev. Lett. **61**, 1819 (1988).
[55] T. Alexopoulos *et al.*, Notre Dame University Report No. UND-HE-02-02-90, 1990 (unpublished).